ACS APPLIED MATERIALS & INTERFACES

www.acsami.org

Research Article

Solid-like Behaviors Govern Evaporative Transport in Adsorbed Water Nanofilms

Kimia Montazeri, Mohammad Javad Abdolhosseini Qomi, and Yoonjin Won*

Cite This: https://dx.doi.org/10.1021/acsami.0c13647

Read Online

ACCESS | Metrics & More | Article Recommendations | Supporting Information

ABSTRACT: The thermophysical attributes of water molecules confined in a sub-nanometer thickness significantly differ from those in bulk liquid where their molecular behaviors start governing interfacial physics at the nanoscale. In this study, we elucidate nanothin film evaporation by employing a computational approach from a molecular perspective. As the liquid thickness decreases, the solid-like characteristics of adsorbed water nanofilms make the resistance at solid−liquid interfaces or Kapitza resistance significant. Kapitza resistances not only show a strong correlation with the surface wettability but also dominate the overall thermal resistance during evaporation rather than the resistance at evaporating liquid−vapor interfaces. Once the liquid thickness reaches the critical value of 0.5−0.6 nm, the evaporation kinetics is suppressed due to the excessive forces between the liquid and solid atoms. The understanding of molecular-level behaviors explains how a hydrophilic surface plays a role in determining evaporation rates from an atomistic perspective.

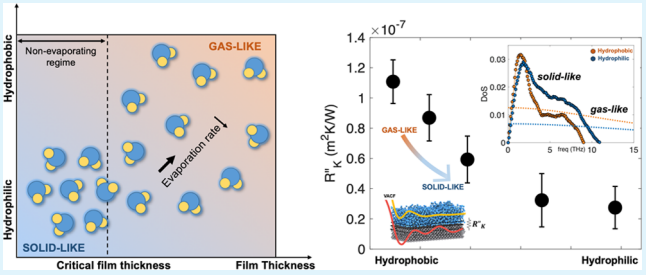

KEYWORDS: *evaporation, water nanofilms, solid-like behaviors, wettability, Kapitza resistance, evaporation resistance*

INTRODUCTION

Surface wettability greatly dominates liquid−vapor phase change that transfers energy in natural, as well as in numerous industrial applications. Various surface wettability can be found in nature, ranging from hydrophobic behaviors—plant leaves, bird feathers, butterfly wings, and spiders' silks—to superhydrophilic surfaces—the gelatin layer on fish skin.[1−3] Engineered surfaces, inspired by biological systems, can promise performance breakthroughs for applications ranging from water-energy systems to electronics cooling, printing surfaces, water filtration, and water-energy harvesting.[4,5] For example, thermal technologies for microelectronics cooling have taken advantage of the use of nanostructures to increase hydrophilicity and associated contact areas for evaporating processes.[6−12] With the presence of nanostructures,[13−15] the liquid thickness is typically constrained down to nanometer lengths, and both the nanofilm thickness and the surface wettability govern the corresponding phase change phenomena.[16−18] Specifically, the liquid thickness at the three-phase (liquid−solid−vapor) contact lines will decrease down to sub-nanometers, where this nanofilm is considered the most efficient phase change regions, over the entire interface, by showing the highest evaporation rates. Therefore, the understanding of nanothin film's phase change process is essential to elaborate interfacial and transport phenomena on nanosurfaces. The mechanisms of phase change within the nanothin water film might differ from bulk properties as the length scales are reduced toward a few nanometers.[19,20] Within a nanothin film, the hydrogen bond network will be disturbed, dynamics of rotational degrees of freedom of water will be slowed down, and water molecules' dipole will be changed compared to that in bulk.[21,22] Such nanoscale phenomena eventually impact the effective thermofluidic characteristics.[23] Despite the significance of understanding the water molecule behaviors constrained in nanoscale configurations, it has been challenging to provide a full description about their nanoconfinement phenomena.[24,25]

While there have been extensive studies to investigate thermal resistances at different types of interfaces by employing experimental analysis,[26] analytical modeling,[27] and numerical simulations,[28,29] traditional experimental approaches[30] become impractical at nanometer scales. Instead, molecular dynamics (MD) simulations can provide a sufficient means to investigate nanoscale interfacial physics from an atomistic perspective.[31,32] The use of MD simulations enables the detailed calculations of thermophysical characteristics across individual phases and interfaces.[33−35] The solid−liquid interfaces are reported with the focus on the surface morphological information,[36−39] chemistry and roughness,[40] nanofilm thickness,[41] molecule

Received: July 29, 2020
Accepted: November 4, 2020

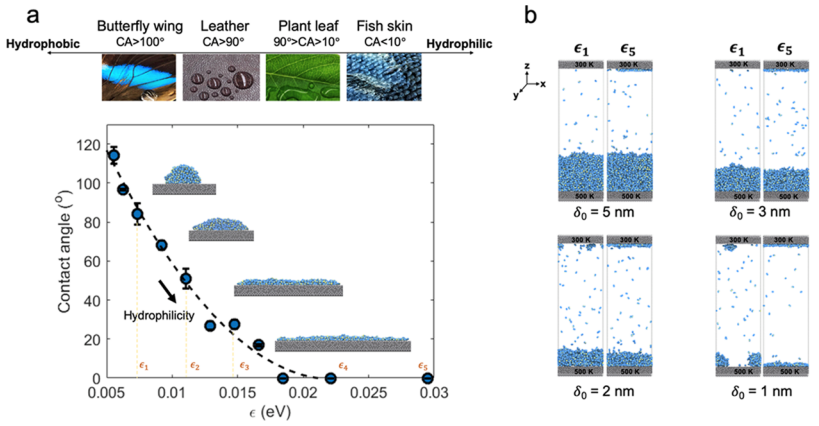

Figure 1. Effects of the surface wettability and film thickness on the contact angle and phase change behavior. (a) By modulating the Lennard-Jones (LJ) energies from 0.005 to 0.025 eV, various surface wetting properties are obtained, spanning from hydrophobic to hydrophilic, which can be correlated with a broad range of biological examples such as butterfly wings, leather, plant leaves, and fish skin. (b) Snapshots from molecular dynamics (MD) simulations show the evaporation process of various surfaces ranging from neutral (CA = 84°) to hydrophilic surfaces (CA ∼ 0°) with different film thicknesses of 5, 3, 2, and 1 nm at 0.5 ns. To simulate evaporation physics, the top and bottom surfaces are maintained at 500 and 300 K, respectively.

packing levels,[42] or their wettability,[43−46] while the solid−liquid interfaces are influenced by phonon scattering mismatches.[47−50] It has been reported that thermal resistances at solid−liquid interfaces for thin liquid films in the range of nanometers are comparable to those at solid−solid interfaces.[51,52] The majority of the previous studies has merely focused on the thermal transport between a solid and liquid without phase change.[49,53−55]

The solid−liquid interfacial resistances have drawn attention during phase change phenomena.[56−62] One example shows that the evaporation rate increases as solid−liquid thermal resistances decrease, by investigating an argon droplet on a heated substrate through MD models.[14] The findings available from previous studies confirm that surface morphology and wettability can affect phase change physics; however, the mechanisms to explain the impact of interfacial physics on evaporation transport properties[63] are not well-explored. In addition, the understanding about detailed behaviors of water molecules constrained in nanometer-thick liquid films is still lacking.

The computational technique applied to water molecule systems is presented in this paper, along with the focus on molecular-level interactions. In this context, MD models are employed to understand the mechanisms that govern evaporation phenomena of nanothin water films, by testing various surface inputs. The liquid film thicknesses in this study range from 5 to 1 nm, where the sub-nanometer thickness is suggested to understand the effects of intermolecular forces between solid and liquid molecules when they are confined in a nanothin film. Tracking of molecule numbers enables us to identify different regimes during the evaporation process; the onset, the steady, and the suppressed regimes. The interfacial characteristics such as translational dynamics of the molecules are carefully investigated with thermal resistance values, by calculating the density of states (DoS) and their decomposition into gas- and solid-like components. The study of the interfacial phenomena at solid−liquid or liquid−vapor interfaces provides insights toward molecule vibration-dominated thermal transport during the phase change processes. New discoveries about the nanothin water films, which serves as the main objective of this paper, can greatly benefit many water-based applications where water-surface properties are critical.

Design of Molecular Dynamics Models. In this study, MD simulations are performed using the large-scale atomic/molecular massively parallel simulator (LAMMPS).[64] The models account for liquid−solid−vapor interactions at an elevated temperature, allowing us to calculate thermal resistances through each phase or interface. To do this, solid atoms are arranged in a face centered cubic (FCC) structure with a lattice parameter of 3.615 Å. The solid−solid interactions are modeled using the embedded atom model (EAM).[65] The water molecules are represented with the TIP4P water model, which allocates two sites for hydrogen atoms that possess positive charges and one site for the oxygen atom. The negative charge of the oxygen atom is placed at the fourth site, which is located at a short distance from the oxygen atom, along the bisector of the H−O−H angle. SHAKE algorithm keeps the harmonic O−H and H−H bonds and H−O−H angle rigid, which prevents the vibrational motions of the water molecules in the system. Lennard-Jones (LJ) potential with a cutoff distance of 12 Å describes the interactions between oxygen and solid atoms or the oxygen−oxygen interactions, where long-range coulombic interactions are calculated using the particle−particle−particle−mesh (PPPM) solver.[66] The values of ε (LJ interaction energy, i.e., van der Waals interaction) between the oxygen and solid atoms are tuned in a wide range to represent wetting behaviors spanning from the neutral surface with a contact angle of 84° (ε_1 = 0.0073 eV) to hydrophilic surfaces (ε_2 = 0.0110 eV, ε_3 = 0.0147 eV, ε_4 = 0.0221 eV, and ε_5 = 0.0294 eV). For simplicity, the value of σ (LJ distance between oxygen and solid atoms) is kept constant σ_{Cu-O} = 2.75185 Å for all of the studied surfaces.[67]

Three different unit cells are defined in this paper, and each cell is used to study specific properties: cell 1 characterizes the contact angle of a water droplet on various surfaces; cell 2 is designed to examine evaporative phase change using non-equilibrium molecular dynamics (NEMD) simulations; and cell 3 is used to compute the density of states using equilibrium molecular dynamics (EMD) simulations. See SI.1 for the detailed settings of each cell along with the dimensions and

https://dx.doi.org/10.1021/acsami.0c13647
ACS Appl. Mater. Interfaces XXXX, XXX, XXX−XXX

number of molecules. In all simulations, we discretize the simulation cell into small three-dimensional (3D) grids of 4 Å × 4 Å × 4 Å and calculate the values of thermophysical properties, such as kinetic and potential energies, densities, and temperature, which is averaged for all particles within each grid. The grid size ensures that each grid is large enough to contain at least one water molecule, and the properties of each molecule are considered once, in the averaging process.[35]

To quantify the effects of bond strength on the wetting properties, first we measure the contact angle of a water droplet in contact with each surface by cell 1. cell 1 is a periodic cell that has a water droplet of 1107 water molecules on a flat solid surface of 9600 solid atoms. The van der Waals interaction ε between the oxygen and solid atoms is tuned, ranging from 0.005 to 0.025 eV to represent various surface wettability available in nature. (see Figure 1a). For each ε value, cell 1 is relaxed at 300 K for 1 ns in the NVT ensemble (constant number of particles, constant volume, and constant temperature) with a time step of 1 fs. After the relaxation, the droplet contact angles on the surface are computed, where the contact angle is defined as the angle between the surface and the tangent line to the droplet surface at the contact point.[68,69] The contact angles are calculated by fitting a second-order polynomial function to the water droplet at the right and left sides of its contact region with the solid surface. The tangent lines to the polynomial function are then obtained where the contact angles are the angles between the tangent lines and the solid surface. Error bars in Figure 1a correspond to the standard deviations of obtained contact angles at both sides. See SI.2 for more details on the contact angle calculation. Figure 1a shows how the van der Waals interaction changes the contact angle of a water droplet. For example, a water droplet on a copper surface shows a contact angle of almost 84°. Increasing the van der Waals interaction in this range decreases the contact angles to almost 0°. The figure insets show how droplets form on each surface. The contact angles for the various van der Waals interactions show a good agreement with previously reported values from the literature.[67,70,71]

Once the surface wettability is characterized, we investigate the evaporation physics related to the rates associated with phase change using cell 2, with dimensions of 7.23 nm × 3.61 nm × 22.92 nm in the x, y, and z directions, consists of 6400 atoms in the solid substrates at the top and the bottom of the simulation cell. The two outermost layers of solid surfaces are fixed to keep the volume of the cell constant. As shown in Figure 1b, for different simulations, a thin water film with thicknesses of 5, 3, 2, and 1 nm consisting of 4350, 2610, 1740, and 626 water molecules, respectively, is placed on the solid surface at the bottom. Periodic boundary conditions in all directions are applied to ensure particle interactions across the boundary of the unit cell. Due to the small thicknesses of nanothin films, the effects of gravitational forces on the water films in all cases are much smaller compared to other types of attraction forces such as van der Waals and will be negligible. A time step of 1 fs is chosen for the computations to ensure the stability of the motion of molecules and conservation of energy.

To study the evaporation phenomena for various surface types and different water film thicknesses, each system is first equilibrated for 1 ns in the NVT ensemble, where the temperature of the system is maintained at 300 K using the Nosé–Hoover thermostat. Then, the phase change process of the water film is performed in a constant-energy, constant-volume ensemble (NVE) under elevated temperature in the bottom. Berendsen thermostats maintain the temperature of the bottom surface at 500 K, which acts as an evaporator, and the temperature of the top surface at 300 K, which collects the evaporated water molecules (Figure 1b). These thermostats at the top and bottom create a temperature gradient between the evaporator and condenser. This temperature gradient leads to a constant heat flux across the system, which enables the phase change process. The heat flux is calculated by recording the accumulated heat across the system due to the presence of the thermostats at both ends of the simulation cell. In this study, the liquid and vapor phases are distinguished based on the density of their neighbor region. The region with the density of 0.4 g/cm^3 is identified as the liquid–vapor interface, separating liquid and vapor phases,[14] separating liquid and vapor phases where the density is equal to the average of liquid (~0.8 g/cm^3) and vapor (~0 g/cm^3). It should be noted that, with the heated boundary condition, liquid–vapor interfaces continuously change and are monitored during the simulations. The solid–liquid interface is defined as the location of the closest water molecules to the solid substrate, ranging between 18 and 22 Å.

To quantify the translational dynamics of water near the solid contact line, the density of states (DoS) is calculated from EMD simulations for different surface types. For this, cell 3 is defined, which is smaller than cell 2 in size to save computational cost and time for different water film thicknesses of 5, 3, 2, and 1 nm. For this, the system is first equilibrated for 1 ns in the NVT ensemble at 300 K. Then, data sets are collected for an additional 20 ps simulation time. Since femtosecond resolution is needed for the calculation of DoS, the velocities of each atom in the system are extracted with time steps of 1 fs. Velocity autocorrelation functions (VACF) are calculated after the simulation runs for 20 ps. The VACFs are obtained for a maximum delay time of 10 ps, therefore each point on the VACF signal is an average value over a time period of 10 ps. It should be noted that the VACF and DoS are calculated for interfacial oxygen and solid atoms within an 8 Å distance from the solid–liquid interface.

Evaporation Phenomena in Nanofilms. Once the surface wettability is characterized, we simulate the transient evaporation performances using cell 2 (Figure 1b). As shown in Figure 1b, the liquid film thickness ranges from 5 to 1 nm, where the sub-nanometer thickness is suggested to understand the effects of intermolecular forces between the solid surface and water molecules; various surface wettability from ε = 0.0073–0.0294 eV is exploited; and the top and bottom surface temperatures are maintained at 500 and 300 K, respectively. It should be noted that for the surface with the 1 nm water film, where the van der Waals interaction between the solid and oxygen atoms is ε_1 = 0.0073 eV, the water film shows the formation of droplets during the equilibrium process, as shown in Figure 1b. Since the average thickness of the water droplet is not uniform, calculations of the thermal resistances and DoS are excluded for this case and only evaporation rates are reported. The simulation outcomes allow us to calculate the evaporation rates by tracking the number of liquid and vapor molecules in the cell[72]

$$\dot{m}''_{MD} = \frac{\Delta N_L}{\Delta t}\frac{M_L}{N_{AV}}\frac{1}{A_{LV}} \quad (1)$$

https://dx.doi.org/10.1021/acsami.0c13647
ACS Appl. Mater. Interfaces XXXX, XXX, XXX–XXX

In this equation, N_L is the liquid molecule number at each time step, Δt is the time interval for which the liquid molecule number is counted. N_{AV}, M_L, and A_{LV} are Avogadro's number, water molar weight, and liquid−vapor interface area, respectively. In all simulations, the time interval of 5 ps is used for the evaporation rate calculation. The representative plots of N_L/N_{total} and corresponding evaporation rates in Figure 2 show distinct changes, which can be categorized into

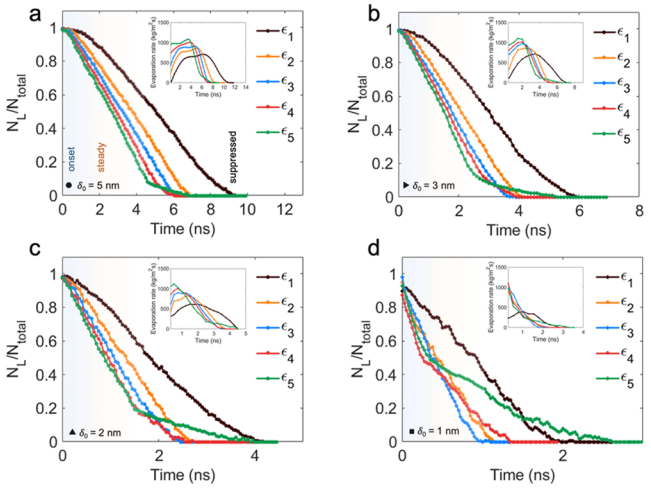

Figure 2. Transient evaporation performances for various surface wettability (ε_1 = 0.0073 eV, ε_2 = 0.0110 eV, ε_3 = 0.0147 eV, ε_4 = 0.0221 eV, and ε_5 = 0.0294 eV). Plots show the changes in the normalized number of liquid molecules to the total liquid molecules, where the slopes of N_L/N_{total} represent the evaporation rates in the insets, for different water thickness of (a)−(d) δ_0 = 5, 3, 2, and 1 nm, respectively. The thicker liquid films exhibit three distinct regimes: the onset, the steady, and the suppressed evaporation regimes. As the thickness decreases or the surface becomes hydrophilic, the onset regime disappears, and the slope rapidly decreases in a prolonged suppressed regime.

three different regimes: (1) In the onset regime, the slope gradually increases starting from 0 at N_L/N_{total} = 1. This increasing trend is attributed to the time required for the liquid molecules in the upper layers to obtain enough energy from the solid atoms to depart the liquid phase. The hydrophilic surfaces show the strong intermolecular forces between the solid and liquid molecules, leading to dense and uniform liquid films (see SI.2) enough to transport energy from the solid to liquid molecules. On the other hand, the liquid molecules are loosely packed near neutral surfaces, so additional time is required to transport energy to upper liquid molecules, which means a slow evaporation. (2) The steady regime, where the slope of N_L/N_{total} remains a constant over time, corresponds to a near-equilibrium state with a constant evaporation rate. (3) In the suppressed regime, the decrease in the liquid film thickness at the bottom surface leads to a suppressed evaporation rate that eventually decreases to 0. This is related to the pronounced attractive forces between interfacial water molecules on a solid surface and is studied in more details in later sections.

The observation of three regimes is clear for the thicker liquid films or neutral surfaces in Figure 2a,b, where the attractive forces between the liquid and solid molecules are relatively weak. As the film thickness decreases or the surface becomes hydrophilic in Figure 2c,d, the onset regime as well as the steady regime disappears, and the suppressed regime begins at the earlier stage. Therefore, the maximum evaporation rate of ~1000 kg/(m^2 s) occurs at the beginning. The 1 nm film evaporation is mainly composed of the suppressed regime.

The effects of surface wetting properties on the regime-averaged thickness (that is averaged over time for each regime distinguished by the slope of N_L/N_{total}) are examined, as Figure 3 shows the normalized regime-averaged thickness for

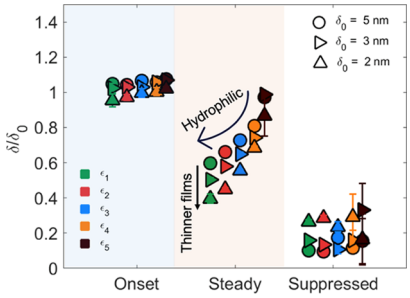

Figure 3. Normalized water film thickness averaged for each evaporation regime. In the onset regime, the thickness remains the same as its initial value of 1 because of a slow evaporation. In the steady regime, the heat is being uniformly transferred to all of the liquid molecules, and this process is mainly governed by surface wettability. In the suppressed regime, the evaporation rate slowly decreases toward 0 due to the strong intermolecular forces between the liquid and solid molecules. The critical thickness δ_c in the suppressed regime is in the order of only two water layers, which is 0.5−0.6 nm, for all cases, regardless of the surface wetting properties and initial thicknesses. The error bars correspond to the deviations along the x-direction in the simulation cell.

all cases. Film thickness is defined as the distance between the liquid−vapor interface and the solid−liquid interface line. The average thicknesses in the steady regime are calculated during the time that the evaporation rate remains within 20% of the maximum value. In Figure 3, the normalized water film thickness in the onset regime does not change from its initial value, which is approximately 1, as most of the water molecules have not received enough energy from the heat source yet. The thickness in the steady regime decreases as the water molecules constantly evaporate. This means that hydrophilic surfaces show a smaller thickness due to a higher evaporation rate. The water film thickness in the suppressed regime is almost the same for all cases, referred to as the critical thickness δ_c in this work. The δ_c exists because of the strong intermolecular forces between the solid and liquid molecules, resulting in a slow evaporation. The average δ_c is about 0.5−0.6 nm, representing two layers of water molecules. The computational results on transient evaporation rates suggest attaining hydrophilicity for the stable and reliable evaporations.

Solid-like Behaviors of Nanofilms. To better understand how thermal energy transports through different phases during the evaporation, we further examine the atomistic motions near the contact lines by measuring the density of states (DoS)[73−75] in cell 3, by exploiting the velocity autocorrelation function (VACF) for the solid or oxygen atoms near interfaces.[58,76] The Fourier transform of the VACF provides the DoS function

$$\mathrm{DoS}(\nu) = \int \frac{\langle v(t)\cdot v(0)\rangle}{\langle v(0)\cdot v(0)\rangle} e^{-2\pi i\nu t} dt \quad (2)$$

https://dx.doi.org/10.1021/acsami.0c13647
ACS Appl. Mater. Interfaces XXXX, XXX, XXX−XXX

Analysis of the DoS measures the motion of particles in the frequency domain from an atomistic perspective, which can provide the insights into the kinetics and thermodynamics of molecules at the interface.[59] The DoS of a fluid can be decomposed into gas- and solid-like components using the two-phase thermodynamic model (2PT)[77,78]

$$\mathrm{DoS}\ (\nu) = S_{\mathrm{gas-like}}\ (\nu) + S_{\mathrm{solid-like}}\ (\nu) \tag{3}$$

where $S_{\mathrm{gas\text{-}like}}(\nu)$ and $S_{\mathrm{solid\text{-}like}}(\nu)$ represent all of the diffusive components and all nondiffusive characteristics, respectively. The gas-like component is assumed to follow the hard-sphere model[78]

$$S_{\mathrm{gas-like}}(\nu) = \frac{S^0}{1 + \left[\frac{\pi S^0 \nu}{6 f N}\right]^2} \tag{4}$$

where S^0 is the density of state at zero frequency, f is the fluidicity parameter, and N is the number of molecules in the system. The fluidicity parameter spans between zero and unity to represent both the absolute nondiffusive solid-like behavior and in contrast the complete diffusive ideal gas behavior. By using the 2PT model, we determine the thermodynamic properties of a fluid as well as the fluidicity parameter f for each surface. Based on this, a universal equation for the fluidicity is calculated as[78]

$$2\Delta^{-9/2} f^{15/2} - 6\,\Delta^{-3} f^{5} - \Delta^{-3/2} f^{7/2} + 6\,\Delta^{-3/2} f^{5/2} + 2f - 2 = 0 \tag{5}$$

where Δ is the nondimensional diffusivity constant. Nondimensional diffusivity constant is a function of temperature, volume, the number of particles in the system, mass of the particles, and the density of states at zero frequency. Therefore, Δ can be obtained by

$$\Delta(T, V, N, m, S^0) = \frac{2S^0}{9N}\left(\frac{\pi kT}{m}\right)^{1/2}\left(\frac{N}{V}\right)^{1/3}\left(\frac{6}{\pi}\right)^{2/3} \tag{6}$$

where T, V, and N represent the temperature, the volume, and the number of particles in the system, respectively, while k is the Boltzmann constant and S^0 is the value of DoS at zero frequency. From this equation, Δ can be simply found using measurable features of the system such as temperature, volume, and the number of particles. Further, the value of the fluidicity parameter can be found by solving eq 5 based on the obtained Δ.[78]

The DoS functions in liquid films are shown to display a peak at low frequencies due to the weak van der Waals interactions between water molecules. In contrast, the solid-like DoS functions have a peak at higher frequencies (see SI.5), where the peaks are related to the vibrations of solid atoms. In addition, the solid-like component should be 0 at frequency = 0, whereas the gas-like component possesses a nonzero value at the same position. The decomposition of the DoS into gas and solid-like components is essential for separating the diffusional and vibration contributions. The finite value at zero frequency is therefore a measure for the level of diffusivity of the system.[77] Using the 2PT model, some degrees of freedom of the atoms are associated with solid-like behaviors using harmonic oscillator assumption, while some degrees of freedom are related to gas-like behaviors using hard-sphere assumption. Figure 4 shows the decomposed density of states (DoS) function into solid- and gas-like components for

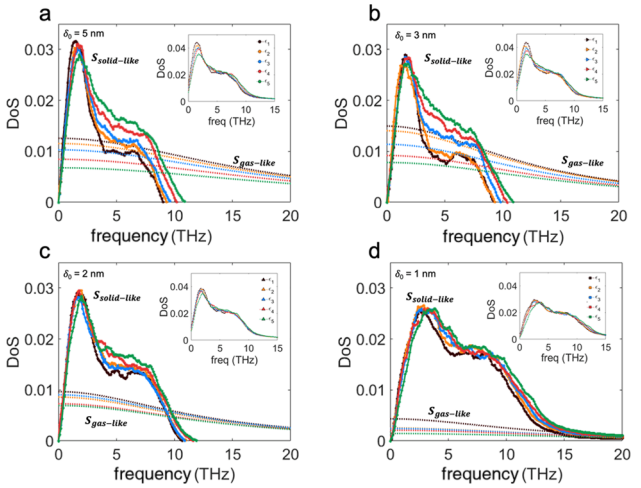

Figure 4. Solid- and gas-like components of density of states (DoS) function for (a–d) δ_0 = 5, 3, 2, and 1 nm, respectively. The insets show the total DoS function before the decomposition. (a–c) As the surface becomes hydrophilic, the peak of the solid-like component (solid line) slightly decreases and gets shifted to higher frequencies, whereas the gas-like component (dash line) dramatically decreases. The results suggest that the effect of surface wettability on molecular behaviors is critical. (d) Gas-like component in the 1 nm water film shows much smaller values, which supports the notion of solid-like characteristics in the sub-nanometer thin films.

different water film thicknesses on various surfaces. The total DoS functions before the decomposition for all cases are calculated in the insets of Figure 4. The solid-like component starts from zero at zero frequency, whereas the gas-like component possesses a nonzero value at the same position. For the hydrophilic surfaces, the peak of the solid-like components slightly decreases and gets shifted to higher frequencies, while the values of the gas-like component dramatically decrease. For more hydrophilic surfaces, the gas-like component of the DoS starts with lower values compared to the neutral surface.

Such solid-like behaviors on hydrophilic surfaces are attributed to the strong bonds between the surface and water molecules. As the liquid film thickness decreases down to two layers of water molecules, thinner films have much smaller gas-like component values, proving the dominant solid-like behaviors. The molecular behaviors support the presence of the critical liquid film thickness during the extended suppressed evaporation regime, explained in the earlier section. These findings are listed in the regime map in the abstract figure.

Interfacial Thermal Resistance Analysis. As the liquid film thickness decreases, molecular vibrational mismatches at the interface play a key role in determining the overall transport physics instead of conduction through liquid or solid phases. An equivalent thermal circuit that represents heat transfer in the cell is illustrated in Figure 5a inset, which consists of (1) conduction resistance through the solid surface $R''_{c,s}$ (which is not considered in this study), (2) resistance through the solid–liquid interface R''_{K}, (3) conduction resistance through the liquid $R''_{c,l}$, and (4) resistance associated with evaporation at the liquid–vapor interface R''_{evap}. The overall thermal resistance can be calculated using the temperature gradient from the evaporator to the vapor phase divided by the overall heat flux, resulting in the values of 3.7×10^{-7} and 4.9×10^{-7} m^{2}K/W. The temperature distributions in

https://dx.doi.org/10.1021/acsami.0c13647
ACS Appl. Mater. Interfaces XXXX, XXX, XXX–XXX

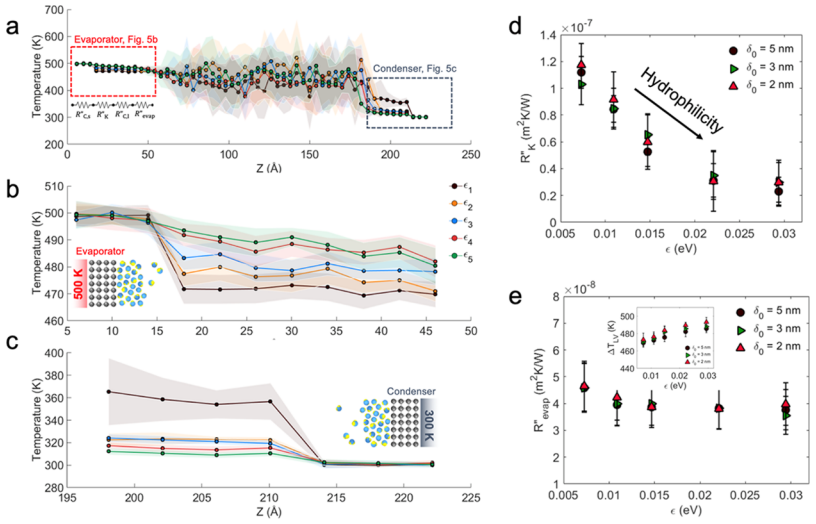

Figure 5. Temperature profile along the domain during the evaporation of a 5 nm water film. (a) Temperature profiles in the *z*-direction are shown for various surface wetting properties. The evaporator (left) and the condenser section (right) correspond to the high temperature (500 K) and low temperature (300 K). The representative data is averaged over the steady-state region. Standard deviations are shown with colored shades for each surface. Plots show the detailed view of the temperature profile in the (b) evaporator and (c) condenser sections. Temperature discontinuity across the solid−liquid interface is attributed to the interfacial thermal boundary resistance, called the Kapitza resistance, and varies as the surface wettability changes. (d) Discontinuity is attenuated for hydrophilic surfaces due to stronger intermolecular interactions between the solid and water molecules, decreasing the Kapitza resistance. (e) Evaporation resistances show independent values to the surface properties. The temperature differences between the interface T_{lv} and the vapor domain T_v are shown in the inset. The Kapitza resistances are larger than evaporation resistances by almost three times, which dominate the effective thermal resistance.

Figure 5a allow us to calculate each value of thermal resistances, while Figure 5b,c shows the detailed views of temperature distributions of the evaporator and condenser, respectively. The values of the conduction resistance $R''_{c,l}$ through the liquid range from 1.6×10^{-9} to 8.3×10^{-9} m^{2}K/W, which is much smaller than other interface resistances and will not be considered in this study. See SI.6 for the details.

Discontinuous temperature profiles at the solid−liquid interface are observed because of molecular-level scattering mismatches between those two phases, which can be translated into interfacial thermal boundary resistance, the Kapitza resistance R''_K.[62,79] Kapitza resistance can be calculated using the ratio of the temperature difference across the solid−liquid interface ΔT_{ls} in the steady evaporation regime and heat flux q''. Kapitza resistances range from 2.7×10^{-8} to 1.1×10^{-7} m^{2}K/W in Figure 5d, showing a good agreement with values reported in previous studies.[41,42,67,80,81] This plot shows that the Kapitza resistances decrease because of the solid-like behaviors of water molecules, as the surface becomes hydrophilic. It is evident that no strong dependence on the water film thickness is observed here. This can be because the Kapitza resistance is calculated after the evaporation reaches the steady states, showing the similar range of critical film thickness (Figure 3) that makes a balance between intermolecular attractions and evaporation phenomena regardless of the initial water film thickness. It should be noted that since for 1 nm film on neutral surfaces, the film thickness is nonuniform showing the formation of droplets, the calculations of average film thickness, DoS, and thermal resistances are excluded for this case.

At the liquid−vapor interface, heat is transferred as a result of the exchange of energy between those two phases. The evaporative heat transfer coefficient is defined to represent heat transfer between the liquid and vapor phase during evaporation over the temperature differences

$$h = q''/(T_{lv} - T_v) \tag{7}$$

where T_{lv} and T_v are the temperature of the liquid−vapor interface and vapor domain, respectively. Since the vapor region is enclosed by the evaporator and the condenser at both ends of the system, the temperature of the vapor region T_v is calculated as the average temperature of the hot and cold regions. To evaluate the evaporation performance in each case, the evaporation resistance R''_{evap} is defined in the thermal circuit as the inverse of the evaporative heat transfer coefficient h at the interface. Using the latent heat and evaporative mass flux, the equivalent evaporation resistance can be expressed as

$$R''_{evap} = \frac{T_{lv} - T_v}{m''_{evap} h_{fg}} \tag{8}$$

Figure 5e shows the evaporation resistances at the liquid−vapor interface, which are in the order of 4.6×10^{-8} and 3.7×10^{-8} m^{2}K/W. As the surface becomes more hydrophilic, the temperature difference between the liquid−vapor interface T_{lv} and the vapor temperature T_v slightly increases (see the inset of Figure 5e), as well as the evaporation rates.

Kapitza resistances are larger than evaporation resistances by almost three times and thereby govern the overall thermal resistance. Here, the hydrophilic surface showcases more solid-like behaviors of water molecules in an adsorbed water nanofilm, which eventuates in the decrease in the molecule vibration mismatches between solid and liquid molecules. Therefore, the hydrophilic surface attains smaller Kapitza resistance as well as the total thermal resistance, which implies more efficient heat transfer through phases. Once the liquid thickness is decreased below the critical film thickness, the evaporation is mostly suppressed due to the strong intermolecular attractions between the solid surface and liquid molecules.

https://dx.doi.org/10.1021/acsami.0c13647
ACS Appl. Mater. Interfaces XXXX, XXX, XXX−XXX

CONCLUSIONS

This study reveals the impact of surface interfaces on thermal transport properties during evaporation from an atomistic perspective. For this, we simulate evaporating water molecules in nanothin liquid films by employing molecular dynamics simulations. The time-dependent evaporation phenomena have been classified into three evaporation regimes: the onset, the steady, and the suppressed regimes, suggesting the presence of the critical film thickness ranging from 0.5 to 0.6 nm. Above the critical film thickness, the combination of wettability and hydrophilicity affects evaporation phenomena and thereby overall thermal resistances. Once the liquid thickness is decreased below the critical film thickness, the evaporation is mostly suppressed due to the strong intermolecular attractions between the solid and liquid atoms. The hydrophilicity-driven, solid-like behaviors eventually result in the low values of thermal resistances at the solid−liquid interfaces, called the Kapitza resistances. The Kapitza resistances are almost three times larger than evaporation resistances and thereby govern the effective thermal resistance, which is also mainly dominated by the surface wettability. The understanding about the detailed interface resistances reveals how hydrophilic surfaces significantly improve thin-film evaporation phenomena related to their molecule-level behaviors. This improvement in thermal transport is favorable in many cooling applications and other thermal management systems. In addition, the suppressed regime that is observed during the evaporation from hydrophilic provides a uniform liquid thickness for a longer time. The suppressed regime during the evaporation might postpone dry-outs and prevent consequent damages to the surface. Advances in the fundamental understanding of water nanofilms have direct implications in designing nanostructure-enhanced heat transfer applications where interfacial water properties are dominant.

ASSOCIATED CONTENT

Supporting Information

The Supporting Information is available free of charge at https://pubs.acs.org/doi/10.1021/acsami.0c13647.

Detailed settings of simulations; contact angle measurement; 3D grid for thermophysical properties; density profiles; velocity autocorrelation functions for calculating DoS; DoS of solid surface; temperature distributions in the steady regime; evaporation rates for all cases in the steady regime (PDF)

AUTHOR INFORMATION

Corresponding Author

Yoonjin Won − *Department of Mechanical and Aerospace Engineering, University of California Irvine, Irvine, California 92697, United States;* orcid.org/0000-0002-8838-6213; Email: won@uci.edu

Authors

Kimia Montazeri − *Department of Mechanical and Aerospace Engineering, University of California Irvine, Irvine, California 92697, United States*

Mohammad Javad Abdolhosseini Qomi − *Department of Civil and Environmental Engineering, University of California Irvine, Irvine, California 92697, United States;* orcid.org/0000-0001-6911-0994

Complete contact information is available at: https://pubs.acs.org/10.1021/acsami.0c13647

Author Contributions

Y.W. proposed and supervised the project, K.M. carried out the simulations, performed the computations, and analyzed the data. M.J.A.Q. advised the conceptual ideas and were involved in planning and supervising. K.M. and Y.W. wrote the manuscript with help from M.J.A.Q. All of the authors participated in discussions of the research.

Notes

The authors declare no competing financial interest.

ACKNOWLEDGMENTS

This work was sponsored by the National Science Foundation (NSF) (Grant No. CBET-TTP 1752147, Thermal Transport Processes). M.J.A.Q. was supported by the NSF (Grant No. 1826122). K.M. is thankful for the financial support from the UC Irvine Mechanical and Aerospace Engineering Department Graduate Fellowship.

REFERENCES

(1) Neinhuis, C.; Barthlott, W. Characterization and Distribution of Water-Repellent, Self-Cleaning Plant Surfaces. *Ann. Bot.* **1997**, *79*, 667−677.

(2) Bormashenko, E.; Bormashenko, Y.; Stein, T.; Whyman, G.; Bormashenko, E. Why Do Pigeon Feathers Repel Water? Hydrophobicity of Pennae, Cassie-Baxter Wetting Hypothesis and Cassie-Wenzel Capillarity-Induced Wetting Transition. *J. Colloid Interface Sci.* **2007**, *311*, 212−216.

(3) Gao, X.; Jiang, L. Water-Repellent Legs of Water Striders. *Nature* **2004**, *432*, No. 36.

(4) Su, X.; Hao, D.; Li, Z.; Guo, X.; Jiang, L. Design of Hierarchical Comb Hydrophilic Polymer Brush (HCHPB) Surfaces Inspired by Fish Mucus for Anti-Biofouling. *J. Mater. Chem. B* **2019**, *7*, 1322−1332.

(5) Liu, X.; Liang, Y.; Zhou, F.; Liu, W. Extreme Wettability and Tunable Adhesion: Biomimicking beyond Nature? *Soft Matter.* **2012**, *8*, 2070−2086.

(6) Fernández, A.; Francone, A.; Thamdrup, L. H.; Johansson, A.; Bilenberg, B.; Nielsen, T.; Guttmann, M.; Sotomayor Torres, C. M.; Kehagias, N. Design of Hierarchical Surfaces for Tuning Wetting Characteristics. *ACS Appl. Mater. Interfaces* **2017**, *9*, 7701−7709.

(7) Bigham, S.; Fazeli, A.; Moghaddam, S. Physics of Microstructures Enhancement of Thin Film Evaporation Heat Transfer in Microchannels Flow Boiling. *Sci. Rep.* **2017**, *7*, No. 44745.

(8) Plawsky, J. L.; Fedorov, A. G.; Garimella, S. V.; Ma, H. B.; Maroo, S. C.; Chen, L.; Nam, Y. Nano-and Microstructures for Thin-Film Evaporation-A Review. *Nanoscale Microscale Thermophys. Eng.* **2014**, *18*, 251−269.

(9) Montazeri, K.; Lee, H.; Won, Y. Microscopic Analysis of Thin-Film Evaporation on Spherical Pore Surfaces. *Int. J. Heat Mass Transfer* **2018**, *122*, 59−68.

(10) Hu, H.; Weibel, J. A.; Garimella, S. V. Role of Nanoscale Roughness in the Heat Transfer Characteristics of Thin Film Evaporation. *Int. J. Heat Mass Transfer* **2020**, *150*, No. 119306.

(11) Liu, R.; Liu, Z. Rapid Thermal Transport at Rough Solid-Fluid Interface: Evaporation and Explosive Boiling on Concave Nanostructure. *Int. J. Heat Mass Transfer* **2020**, *154*, No. 119676.

(12) Lu, Z.; Narayanan, S.; Wang, E. N. Modeling of Evaporation from Nanopores with Nonequilibrium and Nonlocal Effects. *Langmuir* **2015**, *31*, 9817−9824.

(13) Huang, Y.; Jiang, L.; Li, B.; Premaratne, P.; Jiang, S.; Qin, H. Study Effects of Particle Size in Metal Nanoink for Electrohydrodynamic Inkjet Printing through Analysis of Droplet Impact Behaviors. *J. Manuf. Processes* **2020**, *56*, 1270−1276.

(14) Yu, J. J.; Tang, R.; Li, Y. R.; Zhang, L.; Wu, C. M. Molecular Dynamics Simulation of Heat Transport through Solid-Liquid

Interface during Argon Droplet Evaporation on Heated Substrates. *Langmuir* **2019**, *35*, 2164−2171.
(15) Shan, L.; Ma, B.; Li, J.; Dogruoz, B.; Agonafer, D. Investigation of the Evaporation Heat Transfer Mechanism of a Non-Axisymmetric Droplet Confined on a Heated Micropillar Structure. *Int. J. Heat Mass Transfer* **2019**, *141*, 191−203.
(16) Sharma, S.; Debenedetti, P. G. Evaporation Rate of Water in Hydrophobic Confinement. *Proc. Natl. Acad. Sci. U.S.A.* **2012**, *109*, 4365−4370.
(17) Li, Y.; Alibakhshi, M. A.; Zhao, Y.; Duan, C. Exploring Ultimate Water Capillary Evaporation in Nanoscale Conduits. *Nano Lett.* **2017**, *17*, 4813−4819.
(18) Pham, Q. N.; Zhang, S.; Montazeri, K.; Won, Y. Droplets on Slippery Lubricant-Infused Porous Surfaces: A Macroscale to Nanoscale Perspective. *Langmuir* **2018**, *34*, 14439−14447.
(19) Tripathy, M. K.; Mahawar, D. K.; Chandrakumar, K. R. S. Effect of Nano-Confinement on the Structure and Properties of Water Clusters: An Ab Initio Study. *J. Chem. Sci.* **2020**, *132*, No. 7.
(20) Sun, J.; Wang, W.; Wang, H. S. Dependence of Nanoconfined Liquid Behavior on Boundary and Bulk Factors. *Phys. Rev. E* **2013**, *87*, No. 023020.
(21) Qomi, M. J. A.; Bauchy, M.; Ulm, F. J.; Pellenq, R. J. M. Anomalous Composition-Dependent Dynamics of Nanoconfined Water in the Interlayer of Disordered Calcium-Silicates. *J. Chem. Phys.* **2014**, *140*, No. 054515.
(22) Masoumi, S.; Zare, S.; Valipour, H.; Abdolhosseini Qomi, M. J. Effective Interactions between Calcium-Silicate-Hydrate Nanolayers. *J. Phys. Chem. C* **2019**, *123*, 4755−4766.
(23) Mallamace, F.; Corsaro, C.; Mallamace, D.; Vasi, S.; Vasi, C.; Stanley, H. E. Thermodynamic Properties of Bulk and Confined Water. *J. Chem. Phys.* **2014**, *141*, No. 249903.
(24) Wu, K.; Chen, Z.; Li, J.; Li, X.; Xu, J.; Dong, X. Wettability Effect on Nanoconfined Water Flow. *Proc. Natl. Acad. Sci. U.S.A.* **2017**, *114*, 3358−3363.
(25) Rebay, M.; Kabar, Y.; Kakaç, S. *Microscale and Nanoscale Heat Transfer: Analysis, Design, and Application.*; CRC Press, 2016.
(26) Swartz, E. T.; Pohl, R. O. Thermal Boundary Resistance. *Rev. Mod. Phys.* **1989**, *61*, No. 605.
(27) Kim, B. H.; Beskok, A.; Cagin, T. Molecular Dynamics Simulations of Thermal Resistance at the Liquid-Solid Interface. *J. Chem. Phys.* **2008**, *129*, No. 174701.
(28) Jabbari, F.; Rajabpour, A.; Saedodin, S.; Wongwises, S. Effect of Water/Carbon Interaction Strength on Interfacial Thermal Resistance and the Surrounding Molecular Nanolayer of CNT and Graphene Flake. *J. Mol. Liq.* **2019**, *282*, 197−204.
(29) Heyhat, M. M.; Rajabpour, A.; Abbasi, M.; Arabha, S. Importance of Nanolayer Formation in Nanofluid Properties: Equilibrium Molecular Dynamic Simulations for Ag-Water Nanofluid. *J. Mol. Liq.* **2018**, *264*, 699−705.
(30) Miscuglio, M.; Lin, M. L.; Di Stasio, F.; Tan, P. H.; Krahne, R. Confined Acoustic Phonons in Colloidal Nanorod Heterostructures Investigated by Nonresonant Raman Spectroscopy and Finite Elements Simulations. *Nano Lett.* **2016**, *16*, 7664−7670.
(31) Rajabpour, A.; Seif, R.; Arabha, S.; Heyhat, M. M.; Merabia, S.; Hassanali, A. Thermal Transport at a Nanoparticle-Water Interface: A Molecular Dynamics and Continuum Modeling Study. *J. Chem. Phys.* **2019**, *150*, No. 114701.
(32) Martí, J.; Padro, J. A.; Guàrdia, E. Molecular Dynamics Simulation of Liquid Water along the Coexistence Curve: Hydrogen Bonds and Vibrational Spectra. *J. Chem. Phys.* **1996**, *105*, No. 639.
(33) Hu, H.; Sun, Y. Molecular Dynamics Simulations of Disjoining Pressure Effect in Ultra-Thin Water Film on a Metal Surface. *Appl. Phys. Lett.* **2013**, *103*, No. 263110.
(34) Wang, Z. J.; Chen, M.; Guo, Z. Y.; Yang, C. Molecular Dynamics Study on the Liquid-Vapor Interfacial Profiles. *Fluid Phase Equilib.* **2001**, *183*−*184*, 321−329.
(35) Barisik, M.; Beskok, A. Temperature Dependence of Thermal Resistance at the Water/Silicon Interface. *Int. J. Therm. Sci.* **2014**, *77*, 47−54.
(36) Wang, C. S.; Chen, J. S.; Shiomi, J.; Maruyama, S. A Study on the Thermal Resistance over Solid-Liquid-Vapor Interfaces in a Finite-Space by a Molecular Dynamics Method. *Int. J. Therm. Sci.* **2007**, *46*, 1203−1210.
(37) Hasan, M. R.; Vo, T. Q.; Kim, B. Manipulating Thermal Resistance at the Solid-Fluid Interface through Monolayer Deposition. *RSC Adv.* **2019**, *9*, 4948−4956.
(38) Wang, B. B.; Xu, Z. M.; Wang, X. D.; Yan, W. M. Molecular Dynamics Investigation on Enhancement of Heat Transfer between Electrified Solid Surface and Liquid Water. *Int. J. Heat Mass Transfer* **2018**, *125*, 756−760.
(39) Soussi, J.; Volz, S.; Palpant, B.; Chalopin, Y. A Detailed Microscopic Study of the Heat Transfer at a Water Gold Interface Coated with a Polymer. *Appl. Phys. Lett.* **2015**, *106*, No. 093113.
(40) Acharya, H.; Mozdzierz, N. J.; Keblinski, P.; Garde, S. How Chemistry, Nanoscale Roughness, and the Direction of Heat Flow Affect Thermal Conductance of Solid-Water Interfaces. *Ind. Eng. Chem. Res.* **2012**, *51*, 1767−1773.
(41) Yenigun, O.; Barisik, M. Effect of Nano-Film Thickness on Thermal Resistance at Water/Silicon Interface. *Int. J. Heat Mass Transfer* **2019**, *134*, 634−640.
(42) Alexeev, D.; Chen, J.; Walther, J. H.; Giapis, K. P.; Angelikopoulos, P.; Koumoutsakos, P. Kapitza Resistance between Few-Layer Graphene and Water: Liquid Layering Effects. *Nano Lett.* **2015**, *15*, 5744−5749.
(43) Ramos-Alvarado, B.; Kumar, S.; Peterson, G. P. Solid-Liquid Thermal Transport and Its Relationship with Wettability and the Interfacial Liquid Structure. *J. Phys. Chem. Lett.* **2016**, *7*, 3497−3501.
(44) Murad, S.; Puri, I. K. Thermal Transport across Nanoscale Solid-Fluid Interfaces. *Appl. Phys. Lett.* **2008**, *92*, No. 133105.
(45) Issa, K. M.; Mohamad, A. A. Lowering Liquid-Solid Interfacial Thermal Resistance with Nanopatterned Surfaces. *Phys. Rev. E* **2012**, *85*, No. 031602.
(46) Hu, M.; Goicochea, J. V.; Michela, B.; Poulikakos, D. Water Nanoconfinement Induced Thermal Enhancement at Hydrophilic Quartz Interfaces. *Nano Lett.* **2010**, *10*, 279−285.
(47) Schelling, P. K.; Phillpot, S. R.; Keblinski, P. Kapitza Conductance and Phonon Scattering at Grain Boundaries by Simulation. *J. Appl. Phys.* **2004**, *95*, No. 6082.
(48) Reddy, P.; Castelino, K.; Majumdar, A. Diffuse Mismatch Model of Thermal Boundary Conductance Using Exact Phonon Dispersion. *Appl. Phys. Lett.* **2005**, *87*, No. 211908.
(49) Xue, L.; Keblinski, P.; Phillpot, S. R.; Choi, S. U. S.; Eastman, J. A. Two Regimes of Thermal Resistance at a Liquid-Solid Interface. *J. Chem. Phys.* **2003**, *118*, No. 337.
(50) De Bellis, L.; Phelan, P. E.; Prasher, R. S. Variations of Acoustic and Diffuse Mismatch Models in Predicting Thermal-Boundary Resistance. *J. Thermophys. Heat Transfer* **2000**, *14*, 144−150.
(51) Ardham, V. R.; Leroy, F. Communication: Is a Coarse-Grained Model for Water Sufficient to Compute Kapitza Conductance on Non-Polar Surfaces? *J. Chem. Phys.* **2017**, *147*, No. 151102.
(52) Thekkethala, J. F.; Sathian, S. P. The Effect of Graphene Layers on Interfacial Thermal Resistance in Composite Nanochannels with Flow. *Microfluid. Nanofluid.* **2015**, *18*, 637−648.
(53) Barisik, M.; Beskok, A. Boundary Treatment Effects on Molecular Dynamics Simulations of Interface Thermal Resistance. *J. Comput. Phys.* **2012**, *231*, 7881−7892.
(54) Varshney, V.; Patnaik, S. S.; Muratore, C.; Roy, A. K.; Voevodin, A. A.; Farmer, B. L. MD Simulations of Molybdenum Disulphide (MoS2): Force-Field Parameterization and Thermal Transport Behavior. *Comput. Mater. Sci.* **2010**, *48*, 101−108.
(55) Merabia, S.; Lombard, J.; Alkurdi, A. Importance of Viscoelastic and Interface Bonding Effects in the Thermal Boundary Conductance of Solid-Water Interfaces. *Int. J. Heat Mass Transfer* **2016**, *100*, 287−294.
(56) Han, H.; Schlawitschek, C.; Katyal, N.; Stephan, P.; Gambaryan-Roisman, T.; Leroy, F.; Müller-Plathe, F. Solid-Liquid Interface Thermal Resistance Affects the Evaporation Rate of Droplets from a Surface: A Study of Perfluorohexane on Chromium

https://dx.doi.org/10.1021/acsami.0c13647
ACS Appl. Mater. Interfaces XXXX, XXX, XXX−XXX

Using Molecular Dynamics and Continuum Theory. *Langmuir* **2017**, *33*, 5336−5343.
(57) Hu, H.; Weinberger, C. R.; Sun, Y. Effect of Nanostructures on the Meniscus Shape and Disjoining Pressure of Ultrathin Liquid Film. *Nano Lett.* **2014**, *14*, 7131−7137.
(58) Shavik, S. M.; Hasan, M. N.; Morshed, A. K. M. M.; Islam, M. Q. Molecular Dynamics Study of Effect of Different Wetting Conditions on Evaporation and Rapid Boiling of Ultra-Thin Argon Layer over Platinum Surface. *Procedia Eng.* **2015**, *105*, 446−451.
(59) Fujiwara, K.; Shibahara, M. Local Mass and Energy Transports in Evaporation Processes from a Vapor-Liquid Interface in a Slit Pore Based on Molecular Dynamics. *AIP Adv.* **2018**, *8*, No. 025124.
(60) Nagayama, G.; Kawagoe, M.; Tokunaga, A.; Tsuruta, T. On the Evaporation Rate of Ultra-Thin Liquid Film at the Nanostructured Surface: A Molecular Dynamics Study. *Int. J. Therm. Sci.* **2010**, *49*, 59−66.
(61) Liang, Z.; Biben, T.; Keblinski, P. Molecular Simulation of Steady-State Evaporation and Condensation: Validity of the Schrage Relationships. *Int. J. Heat Mass Transfer* **2017**, *114*, 105−114.
(62) Hu, H.; Sun, Y. Effect of Nanostructures on Heat Transfer Coefficient of an Evaporating Meniscus. *Int. J. Heat Mass Transfer* **2016**, *101*, 878−885.
(63) Zhang, P.; Yuan, P.; Jiang, X.; Zhai, S.; Zeng, J.; Xian, Y.; Qin, H.; Yang, D. A Theoretical Review on Interfacial Thermal Transport at the Nanoscale. *Small.* **2018**, *14*, No. 1702769.
(64) Plimpton, S. Fast Parallel Algorithms for Short-Range Molecular Dynamics. *J. Comput. Phys.* **1995**, *117*, 1−19.
(65) Mei, J.; Davenport, J. W.; Fernando, G. W. Analytic Embedded-Atom Potentials for Fcc Metals: Application to Liquid and Solid Copper. *Phys. Rev. B* **1991**, *43*, No. 4653.
(66) Hockney, R. W.; Eastwood, J. W. *Computer Simulation Using Particles*; CRC Press, 1983.
(67) Pham, A. T.; Barisik, M.; Kim, B. H. Interfacial Thermal Resistance between the Graphene-Coated Copper and Liquid Water. *Int. J. Heat Mass Transfer* **2016**, *97*, 422−431.
(68) Raj, R.; Maroo, S. C.; Wang, E. N. Wettability of Graphene. *Nano Lett.* **2013**, *13*, 1509−1515.
(69) Fu, L.; Merabia, S.; Joly, L. What Controls Thermo-Osmosis? Molecular Simulations Show the Critical Role of Interfacial Hydrodynamics. *Phys. Rev. Lett.* **2017**, *119*, No. 214501.
(70) Yang, S.; Zhang, Y.; Chen, L. Molecular Dynamics Study on the Effect of Surface Wettability on the Performance of Water Vapor Condensation. *AIP Adv.* **2019**, *9*, No. 025031.
(71) Nguyen, C. T.; Barisik, M.; Kim, B. Wetting of Chemically Heterogeneous Striped Surfaces: Molecular Dynamics Simulations. *AIP Adv.* **2018**, *8*, No. 065003.
(72) Montazeri, K.; Hao, S.; Abdolhosseini Qomi, M. J.; Won, Y. Molecular Dynamics Investigation of Liquid and Vapor Interactions Near an Evaporating Interface: A Theoretical Genetics Perspective. *Adv. Theory Simul.* **2020**, *3*, No. 2000017.
(73) Bellissima, S.; Neumann, M.; Guarini, E.; Bafile, U.; Barocchi, F. Density of States and Dynamical Crossover in a Dense Fluid Revealed by Exponential Mode Analysis of the Velocity Autocorrelation Function. *Phys. Rev. E* **2017**, *95*, No. 012108.
(74) Hu, L.; Desai, T.; Keblinski, P. Determination of Interfacial Thermal Resistance at the Nanoscale. *Phys. Rev. B* **2011**, *83*, No. 195423.
(75) Carles, R.; Benzo, P.; Pécassou, B.; Bonafos, C. Vibrational Density of States and Thermodynamics at the Nanoscale: The 3D-2D Transition in Gold Nanostructures. *Sci. Rep.* **2016**, *6*, No. 39164.
(76) Balucani, U.; Brodholt, J. P.; Vallauri, R. Analysis of the Velocity Autocorrelation Function of Water. *J. Phys.* **1996**, *8*, No. 6135.
(77) Lin, S. T.; Maiti, P. K.; Goddard, W. A. Two-Phase Thermodynamic Model for Efficient and Accurate Absolute Entropy of Water from Molecular Dynamics Simulations. *J. Phys. Chem. B* **2010**, *114*, 8191−8198.
(78) Lin, S. T.; Blanco, M.; Goddard, W. A. The Two-Phase Model for Calculating Thermodynamic Properties of Liquids from Molecular Dynamics: Validation for the Phase Diagram of Lennard-Jones Fluids. *J. Chem. Phys.* **2003**, *119*, No. 11792.
(79) Duda, J. C.; English, T. S.; Piekos, E. S.; Soffa, W. A.; Zhigilei, L. V.; Hopkins, P. E. Implications of Cross-Species Interactions on the Temperature Dependence of Kapitza Conductance. Phys. Rev. B - Condens. *Phys. Rev. B* **2011**, *84*, No. 193301.
(80) Hu, H.; Sun, Y. Effect of Nanopatterns on Kapitza Resistance at a Water-Gold Interface during Boiling: A Molecular Dynamics Study. *J. Appl. Phys.* **2012**, *112*, No. 053508.
(81) Goicochea, J. V.; Hu, M.; Michel, B.; Poulikakos, D. Surface Functionalization Mechanisms of Enhancing Heat Transfer at Solid-Liquid Interfaces. *J. Heat Transfer* **2011**, *133*, No. 082407.

https://dx.doi.org/10.1021/acsami.0c13647
ACS Appl. Mater. Interfaces XXXX, XXX, XXX−XXX